

3D Atomic Arrangement at Functional Interfaces Inside Nanoparticles by Resonant High-Energy X-ray Diffraction

Valeri Petkov,^{*,†} Binay Prasai,[†] Sarvjit Shastri,[‡] and Tsan-Yao Chen[§]

[†]Department of Physics, Central Michigan University, Mt. Pleasant, Michigan 48859, United States

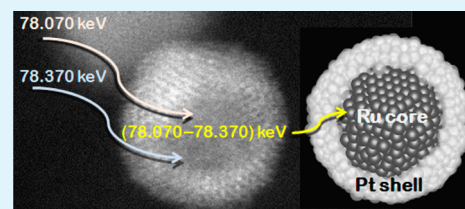
[‡]X-ray Science Division, Advanced Photon Source, Argonne National Laboratory, Argonne, Illinois 60439, United States

[§]Department of Engineering and System Science, National Tsing Hua University, Hsinchu 30013, Taiwan

Supporting Information

ABSTRACT: With current science and technology moving rapidly into smaller scales, nanometer-sized materials, often referred to as NPs, are produced in increasing numbers and explored for numerous useful applications. Evidence is mounting, however, that useful properties of NPs can be improved further and even new NP functionality achieved by not only controlling the NP size and shape but also interfacing chemically or structurally distinct entities into single, so-called “composite” NPs. A typical example is core–shell NPs wherein the synergy of distinct atoms at the core–shell interface endows the NPs with otherwise unachievable functionality. However, though advantageous, the concept of functional interfaces inside NPs is still pursued largely by trial-and-error. That is because it is difficult to assess the interfaces precisely at the atomic level using traditional experimental techniques and, hence, difficult to take control of. Using the core–shell interface in less than 10 nm in size Ru core–Pt shells NPs as an example, we demonstrate that precise knowledge of the 3D atomic arrangement at functional interfaces inside NPs can be obtained by resonant high-energy X-ray diffraction (XRD) coupled to element-specific atomic pair distribution function (PDF) analysis. On the basis of the unique structure knowledge obtained, we scrutinize the still-debatable influence of core–shell interface on the catalytic functionality of Ru core–Pt shell NPs, thus evidencing the usefulness of this nontraditional technique for practical applications.

KEYWORDS: composite metallic nanoparticles for catalytic applications, 3D atomic structure, resonant high-energy X-ray diffraction, element specific atomic pair distribution functions, reverse Monte Carlo simulations



1. INTRODUCTION

Confining materials to nanometer-size dimensions can lead to significant changes in their functional properties. For example, perfectly formed silicon nanospheres not only become harder than bulk silicon but are among the hardest materials known, falling between bulk sapphire and diamond.¹ Another example is Au. While bulk gold is very inert, chemically, a nanoparticles (NPs) of Au catalyze various chemical reactions, including oxidation of toxic CO.² Evidence is mounting that, in addition to controlling the NP size and shape, useful properties of NPs can be improved further, the NP stability can be enhanced, and even new NP functionality can be achieved by interfacing chemically or structurally distinct entities into single structures, often referred to as composite NPs.^{3–6} A typical example is the so-called core–shell NPs, wherein the synergy of distinct atoms at the core–shell interface endows the NPs with otherwise unachievable functionality. For example, nonblinking quantum dots, such as 3 nm CdSe core–thick CdS/SiO₂/Au shell NPs;⁷ efficient metal–semiconductor structures for harvesting solar energy such as 4 nm Ag core–2 nm TiO₂ shell NPs;⁸ devices for controlled drug delivery and release, such as 2 nm FePt core–8 nm CoS₂ shell NPs;⁹ multimodal contrast agents for simultaneous magnetic resonance imaging and X-ray computed tomography, such as <8 nm Fe₃O₄ core–TaO_x shell particles;¹⁰

efficient catalysts for production of hydrogen peroxide (3 M tons/year), such as 10 nm Pd core–Pd₂Hg₅ shell particles;¹¹ building blocks for composites with boosted magneto-static energy, such as 4 nm Fe₅₈Pt₄₂ core–1 nm Fe₃O₄ shell NPs;¹² and others have been fabricated recently. However, though evidently advantageous, the concept of functional interfaces inside NPs, including core–shell type ones, is still pursued largely by trial-and-error. One of the main reasons is that traditional techniques for assessing the three-dimensional (3D) atomic arrangement at internal interfaces in materials, such as grazing incidence X-ray diffraction (GIXD) and small-angle scattering (GISAXS),^{13,14} high-resolution transmission electron microscopy (HR-TEM) coupled to electron energy loss spectroscopy (EELS),^{15,16} high-energy electron diffraction (RHEED),¹⁷ and others, are well suited to planar-type interfaces inside bulk-like crystalline materials only. However, interfaces inside NPs are not necessarily planar, and NPs are not necessarily perfectly crystalline.¹⁸ Besides, typically, NPs are not stacked side-by-side in a periodic manner but are not uniformly deposited on solid supports or dispersed in solutions,

Received: August 12, 2015

Accepted: September 28, 2015

Published: September 28, 2015

and are used in pretty low concentrations.^{19–23} Indeed, it is the inability to obtain precise atomic-level knowledge of interfaces inside actual NPs that currently hampers the utilization of the former for improving the functionality of the latter most. Here, we show that the problem can be solved by employing a nontraditional technique involving resonant high-energy X-ray diffraction (XRD) coupled to atomic pair distribution functions (PDFs) analysis. The technique succeeds by virtue of its high spatial resolution, inherent element specificity and applicability to NPs, including individual NP components (e.g., core and shell components), of any size, shape and atomic-scale structure. As an example, we consider interfaces inside <10 nm Ru core–Pt shell and, for the sake of comparison, Pt–Ru alloy NPs explored for catalytic applications. The reason for choosing these, among many other possible core–shell type catalysts of the Pt–Ru family, as an example is 2-fold. First, catalytic applications are of a high technological importance because, at present, virtually all transportation fuels and most chemicals are produced by processes based on catalysis. Second, Pt–Ru NP catalysts are particularly important for the development of devices for clean energy conversion such as fuel cells, considered vital for meeting the steadily increasing global energy demands. In particular, Ru core–Pt shell NPs have shown a remarkable ability to speed up gas-phase CO oxidation taking place at the anode of Proton Exchange Membrane Fuel Cells (PEMFCs). Note, PEMFC anode catalysts are very much needed since, in the current state of technology, inexpensive hydrogen gas fuelling the cells comes mostly from steam reforming of hydrocarbons. “Reformate” hydrogen, however, contains some impurities such as CO poisoning monometallic Pt NPs typically used as catalysts in PEMFCs, leading to a severe degradation of their performance.^{24–26} In addition, Ru core–Pt shell NPs greatly facilitate alcohol (e.g., ethanol and methanol) electro-oxidation reactions taking place at the anode of direct alcohol fuel cells (DAFCs). Catalysts for DAFC anode are also very much needed because the formation of undesired byproducts of alcohol decomposition has to be minimized by effective C–C bond cleavage and, at the same time, the oxidation of CO species poisoning the reaction has to be accelerated.^{26–29} Pt–Ru alloy NPs have also been found useful as catalysts for the aforementioned reaction, though their activity and stability under fuel cell operating conditions appeared inferior as compared to those of Ru core–Pt shell ones.^{25,26,29,31,32}

Studies have shown that the superb catalytic properties of Ru core–Pt shell NPs are strongly influenced by the 3D arrangement of atoms at the interface between their core and shell components. To assess the influence, various sets of Ru core–Pt shell NPs have been prepared and characterized by a wide range of experimental and computational techniques, including HR-TEM, extended X-ray absorption fine structure spectroscopy (EXAFS), powder XRD, high-energy synchrotron XRD coupled to total atomic PDFs analysis, high-angle annular dark field scanning TEM (HAADF-STEM) imaging, density functional theory (DFT), traditional crystallography-based modeling, and others.^{25,26,29} The great amount of data obtained has been screened by seeking chemical and structural patterns at the Ru core\|Pt shell interface that are consistent with 3D periodic model calculations. As a result, an adequate but largely qualitative atomic-level understanding of Ru core\|Pt shell interface has been achieved.

By contrast, we prepared a well-defined series of Ru core–Pt shell NPs by depositing one, two, and three layers of Pt atoms

on premade Ru cores. Throughout this study, those are referred to as Ru@1Pt, Ru@2Pt, and Ru@3Pt NPs, respectively. The so-prepared Ru core–Pt shell NPs were studied by decisive resonant high-energy XRD carried out at the K edge of Pt atoms. The experimental resonant high-energy XRD data and the element specific atomic PDFs derived from them were not sorted out on the basis of theoretical predictions but let to speak for themselves. In particular, using the experimental PDF data as a guide and not guided by assumptions, we built realistic 3D models of Ru@1Pt, Ru@2Pt, and Ru@3Pt NPs, including the (x,y,z) coordinates of atoms at the Ru core\|Pt shell interface. The models were used to derive precisely all structural characteristics of the interface deemed important to the catalytic properties of Ru core–Pt shell NPs. Special attention was paid to deriving the evolution of Pt–Pt bonding distances and coordination numbers near the interface with the thickness of Pt shell because those are considered crucial for the functioning of Ru core–Pt shell NPs as efficient and stable catalysts.^{25–31} The so-derived structural characteristic of Ru core\|Pt shell interface were used to scrutinize the predictions of current theory dealing with interfaces inside composite NPs, in particular core\|shell type ones. For comparison, we also studied two alloy-type members of the family of Pt–Ru NPs with an overall chemical composition close to that of Ru@1Pt and Ru@3Pt NPs, as described above.

2. EXPERIMENTAL SECTION

Pure Ru cores were synthesized by reducing 100 mM of ruthenium chloride in ethylene glycol. Ru core–Pt shell NPs were then prepared by coating the cores with Pt layers using predesired amounts of $\text{H}_2\text{PtCl}_6 \cdot 6\text{H}_2\text{O}$ (hexachloroplatinic acid). Pt–Ru alloy NPs were prepared by mixing of Platinum(II) acetylacetonate and Ruthenium(II) acetylacetonate in octyl ether solution, and using oleic acid and oleylamine as NP capping agents. Both Ru core–Pt shell and Pt–Ru alloy NPs were deposited on fine carbon powder and postsynthesized treated as to be optimized for catalytic applications. More details of the preparation of Ru cores, Ru core–Pt shell and Pt–Ru alloy NPs are given in the Methods section of the [Supporting Information](#).

The overall chemical composition of Ru core–Pt shell and Pt–Ru alloy NPs was determined by inductively coupled plasma atomic emission spectroscopy (ICP-AES) as described in the Methods section of the [Supporting Information](#). Experiments showed that the overall chemical composition of Ru@1Pt, Ru@2Pt and Ru@3Pt NPs is $\text{Pt}_{30}\text{Ru}_{70}$, $\text{Pt}_{46}\text{Ru}_{54}$ and $\text{Pt}_{60}\text{Ru}_{40}$, respectively. Pt–Ru alloy NPs appeared with an overall composition of $\text{Pt}_{31}\text{Ru}_{69}$ and $\text{Pt}_{75}\text{Ru}_{25}$.

The diameter, hereafter referred to as size, and shape of Ru cores, Ru core–Pt shell and Pt–Ru alloy NPs were determined by TEM experiments described in the Methods section of the [Supporting Information](#). TEM and HR-TEM images showed that Ru@1Pt, Ru@2Pt and Ru@3Pt particles are approximately 3.8 (± 0.4), 4.5 (± 0.4), and 5.1 (± 0.4) nm in size, respectively, and largely spherical in shape ([Figure S1](#)). TEM and HR-TEM imaging ([Figure S2](#)) showed that pure Ru cores, $\text{Pt}_{31}\text{Ru}_{69}$ and $\text{Pt}_{75}\text{Ru}_{25}$ alloy particles are 3.2 (± 0.4) nm, 4.6 (± 0.4) nm and 4.4 (± 0.4) nm in size, respectively, and also largely spherical in shape. Per HR-TEM, both the core–shell and alloy NPs exhibited some surface structural disorder. Such is common for less than 10 nm in size metallic NPs due to finite NP size and NP environment effects.¹⁸

The overall chemical pattern of as-synthesized NPs was examined by HAADF-STEM experiments described in the Methods section of the [Supporting Information](#). HAADF-STEM images shown in [Figure 1](#) (top row) clearly reveal the increasing thickness of Pt shell in the respective core–shell NPs. To cross-check the number of atomic layers in the Pt shell the average size of Ru cores was subtracted from the average size of Ru core–Pt shell NPs, all determined by TEM. The so-obtained independent estimate of Pt shell thicknesses matched well

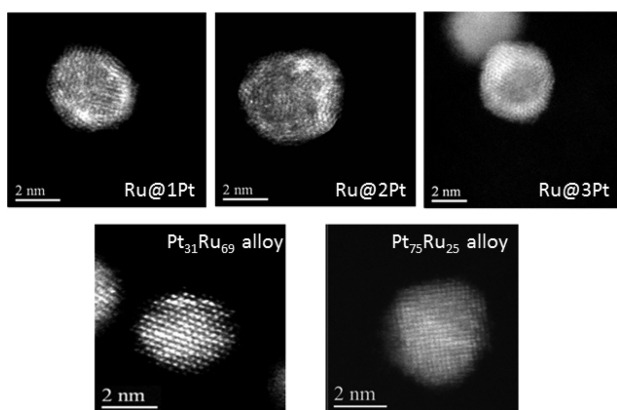


Figure 1. (Top) HAADF-STEM images of carbon supported Ru@1Pt (left), Ru@2Pt (middle) and Ru@3Pt core–shell NPs. The overall chemical composition of the NPs is Pt₃₀Ru₇₀, Pt₄₆Ru₅₄, and Pt₆₀Ru₄₀, respectively. The images show a clear Ru core (dark)–Pt shell (bright) pattern. (Bottom) HAADF-STEM images of carbon supported Pt₃₁Ru₆₉ alloy (left) and Pt₇₅Ru₂₅ alloy (right) type NPs. The former shows an uneven (bright/dark spotted) pattern indicating a partial segregation of Pt (bright spots) and Ru (dark spots) species. The latter is rather uniform, indicating complete alloying of Pt and Ru species in the respective NPs.

the predesired number of Pt atomic layers. HAADF-STEM images shown in Figure 1 (bottom row) indicate that Pt₇₅Ru₂₅ alloy NPs are single phase while Pt₃₁Ru₆₉ alloy NPs are likely partially segregated into Pt- and Ru-rich components. The precise distribution of Ru and Pt species across the NPs studied here, including that at the interfaces inside the NPs, was determined by resonant high-energy XRD

experiments coupled to element specific atomic PDFs analysis described below.

Resonant high-energy XRD experiments were carried out at the 1-ID beamline of the Advanced Photon Source at the Argonne National Laboratory. Essentially such experiments involve collecting two diffraction data sets close to but below the X-ray absorption edge of an atomic species (Figure S3a), taking the difference between these two data sets (Figure S3b), and Fourier transforming it into a quantity called a differential atomic PDF.^{32,33} Similarly to EXAFS,³⁴ the differential PDF reflects only atomic correlations relative to the element whose absorption edge is probed. However, unlike EXAFS, it shows these correlations up to the longest interatomic distance to which they can extend.^{18,35–37} Here we probed the K absorption edge of Pt species (78.395 keV; Figure S3a) not only because of their particular importance to the catalytic properties of Ru–Pt NPs but also for obtaining diffraction data effectively “highlighting” the Pt-based and “dimming” the Ru-based components of the NPs.^{24–31} The latter was critical to determining the 3D atomic arrangement at the interfaces between these components, as described below. More details of the resonant high-energy XRD experiments are given in the Methods section of the Supporting Information. Note, resonant XRD coupled to element specific atomic PDFs analysis has been introduced and employed mostly in structure studies of bulk disordered materials such as glasses and liquids.^{32,33} Here, for the first time ever, we demonstrate that it can be successfully employed for determining the 3D atomic arrangement at functional interfaces inside NPs.

3. RESULTS AND DISCUSSION

Exemplary resonant high-energy XRD patterns for Ru@2Pt NPs are shown in Figure S3b. As can be seen in the Figure the patterns exhibit a few broad, strongly overlapping peaks at low diffraction (Bragg) angles and almost no distinct peaks at high diffraction angles. Resonant high-energy XRD patterns for all other Pt–Ru NPs studied here also appeared poor in sharp

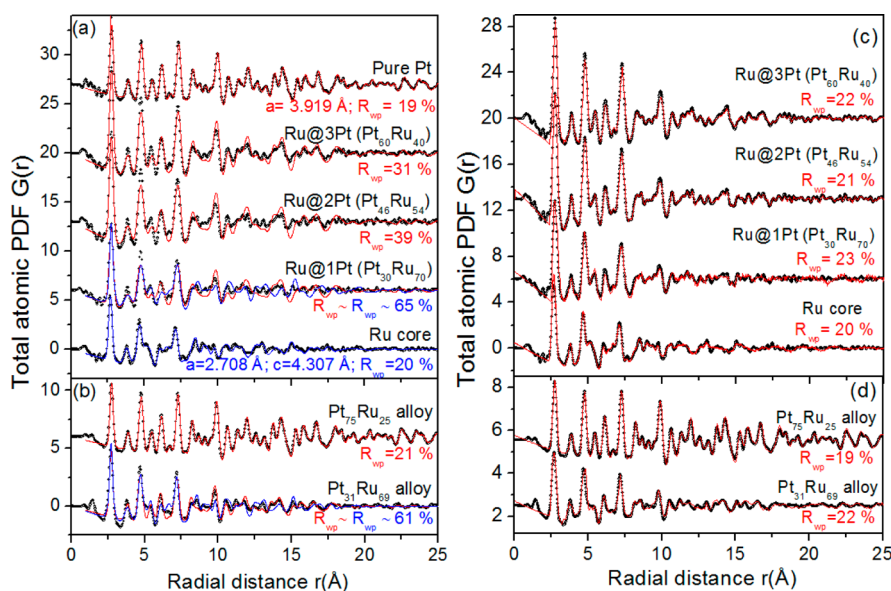


Figure 2. (a) Experimental (symbols) and model total atomic PDFs for pure Ru cores, Ru core–Pt shell and pure Pt NPs. (b) Experimental (symbols) and model (lines) total atomic PDFs for Pt_xRu_{100–x} alloy NPs, where $x = 31$ and 75 . Model PDFs panels a and b are based on (blue line) hexagonal close packed (hcp)- or (red line) face-centered cubic (fcc)-type crystalline lattices. Model refined fcc-lattice parameter for pure Pt NPs and hcp-lattice parameters for pure Ru cores are given by the respective data sets. For reference, the fcc-lattice parameter for bulk Pt is $a = 3.924$ Å and the hcp-lattice parameters for bulk Ru are $a = 2.704$ Å and $c = 4.281$ Å. (c) Experimental (symbols) and model (red line) total atomic PDFs for Ru core–Pt shell and (d) Pt_xRu_{100–x} alloy NPs, where $x = 31$ and 75 . Model PDFs in panels c and d are derived from the respective RMC-refined atomic configurations shown in Figure 4. Model quality indicators, R_{wp} , explained in the Supporting Information, are shown by each data set in color pertaining to the respective model. The number of atomic layers in Pt shell and the overall chemical composition of the NPs is also shown by the respective data sets. Note, all experimental PDFs shown in the figure are obtained from XRD patterns collected using X-rays with the same energy of 78.070 keV.

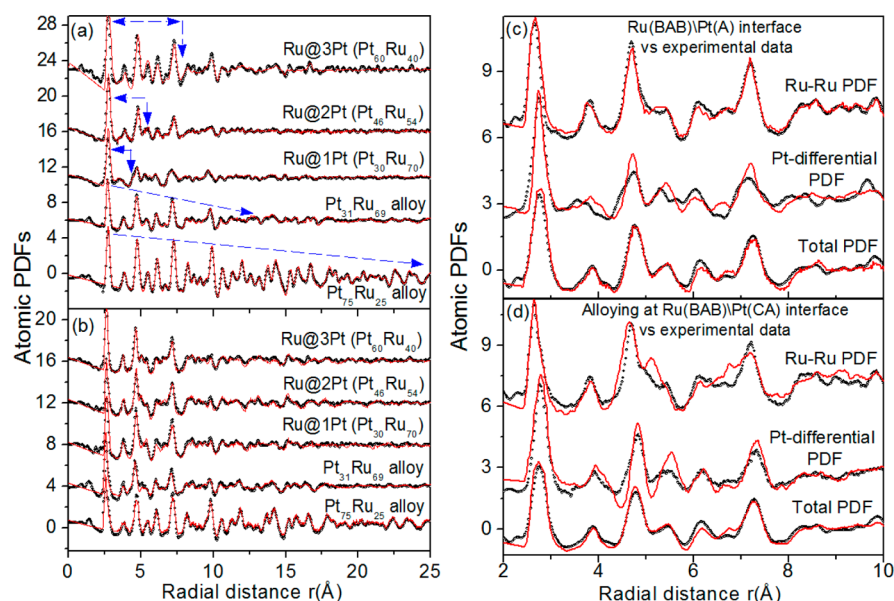


Figure 3. (a) Experimental (symbols) and model (lines in red) Pt-differential PDFs for Ru core–Pt shell and $\text{Pt}_x\text{Ru}_{100-x}$ alloy ($x = 31, 75$) NPs. The number of atomic layers in Pt shell and the overall chemical composition of the NPs is shown by the respective data sets. Straight lines (in blue) emphasize the nearly linear decay of Pt-differential PDFs for Pt–Ru alloy NPs with interatomic distances. Arrows emphasize the sudden decay of Pt-differential PDFs for Ru core–Pt shell NPs with interatomic distances. Model Pt-differential PDFs are derived from the respective RMC-refined atomic configurations shown in Figure 4. (b) Experimental (symbols) and model (lines in red) Ru–Ru partial PDFs for Ru core–Pt shell and $\text{Pt}_x\text{Ru}_{100-x}$ alloy ($x = 31, 75$) NPs. Model partial Ru–Ru PDFs are derived from the respective RMC-refined atomic configurations shown in Figure 4. Quality indicators, R_{wp} , explained in the Supporting Information, for the model-derived PDF data sets in panels a and b are in the range of 22–25%. (c) Experimental (symbols) and model (red line) total, Pt-differential and Ru–Ru partial atomic PDFs for Ru@1Pt NPs wherein the atomic layers at the Ru core/Pt shell interface are stacked in a hcp-type Ru(BAB)\Pt(A) sequence as shown in Figure 5a. (d) Experimental (symbols) and model (red line) total, Pt-differential and Ru–Ru partial atomic PDFs for Ru@2Pt NPs wherein the Pt shell and Ru core are partially alloyed as shown in Figure 5b. Note, all experimental Pt-differential PDFs shown in the Figure are obtained from respective sets of two distinct XRD patterns, one collected using X-rays with energy of 78.070 keV and the other collected using X-rays of energy 78.370 keV. The experimental Ru–Ru PDFs are derived from the experimental total and Pt-differential PDFs as explained in the Methods section of the Supporting Information.

diffraction features. This rendered the well-established, sharp Bragg peaks-based procedures for determining the atomic-scale structure of bulk materials hardly possible to apply to the NPs studied here. That is why the rather diffuse diffraction patterns obtained by resonant high-energy XRD were considered in terms of their Fourier transforms, the so-called atomic PDFs. It has been repeatedly shown that, thanks to the property of Fourier transformation, atomic PDFs derived from diffuse diffraction patterns of NPs show several distinct peaks allowing convenient testing and refinement of atomic-level models for NPs, including metallic ones.^{12,36–38}

Experimental atomic PDFs $G(r)$ derived from single XRD patterns for Ru core–Pt shell NPs and pure Ru cores collected using X-rays with energy of 78.070 keV, which is 325 eV below the K absorption edge of Pt, are shown in Figure 2a,c. For comparison, an atomic PDF for 6 nm in size pure Pt particles, obtained by an independent study, is also shown in Figure 2a. Atomic PDFs $G(r)$ derived from single XRD patterns for Pt–Ru alloy NPs also collected using X-rays with energy of 78.070 keV are shown in Figure 2b,d. By definition,^{18,35} atomic PDFs derived from a single diffraction experiment are referred to as total atomic PDFs since they peak at distances separating all pairs of atoms within the material studied. Accordingly, the total PDFs for Ru core–Pt shell and Pt–Ru alloy NPs shown in Figure 2 peak at distances separating Ru–Ru, Pt–Ru and Pt–Pt pairs of atoms, immediate and all farther neighbors, in the respective NPs. The total PDFs for pure Pt NPs and Ru cores shown in the same Figure peak at distances separating Ru–Ru and Pt–Pt pairs of atoms, respectively.

Experimental atomic PDFs $G(r)$ for Ru core–Pt shell and Pt–Ru alloy NPs derived from respective sets of two distinct XRD patterns, one collected using X-rays with energy of 78.070 keV and the other collected using X-rays with energy of 78.370 keV, are shown in Figure 3a. Note, the latter energy is just 25 eV below the K adsorption edge of Pt. By definition,^{18,32,37} atomic PDFs derived from two diffraction experiments each carried out using X-rays with distinct energy that, however, is as close to the X-ray absorption edge of an atomic species as shown above, are referred to as differential atomic PDFs. Such PDFs are element specific since they peak only at distances specific to the atoms whose adsorption edge has been probed. Accordingly, atomic PDFs shown in Figure 3a are Pt-differential ones and peak at distances separating Pt–Pt and Pt–Ru pairs of atoms in the Ru core–Pt shell and Pt–Ru alloy NPs studied here. Experimental Ru–Ru partial atomic PDFs for Ru core–Pt shell and Pt–Ru alloy NPs, peaking at distances separating Ru–Ru pairs of atoms only, are shown in Figure 3b. For reasons explained below, the experimental total, Pt-differential and Ru–Ru partial PDFs for Ru@1Pt and Ru@2Pt NPs are summarized in Figure 3c,d, respectively. Details of the derivation of total, Pt-differential and Ru–Ru partial atomic PDFs from the experimental resonant high-energy XRD data are given in the Methods section of the Supporting Information.

As shown in Figure 2a, peaks in the experimental total PDFs for all NPs studied here are well-defined, indicating that atoms in the NPs are arranged in well-defined atomic coordination spheres. It has been shown that a sequence of well-defined

atomic coordination spheres can be looked at as a unique structural fingerprint of the material exhibiting it, and hence, it can be used to characterize the overall atomic-scale structure of that material.^{18,35} In particular, the first three peaks in the atomic PDF for pure Pt NPs are positioned at distances of 2.76, 3.90 and 4.80 Å, respectively. The distances are very close to the radii of first, second, and third atomic coordination spheres in bulk Pt adopting a face-centered-cubic (fcc)-type structure.³⁹ The observation indicates that the overall atomic structure of pure Pt NPs is of a fcc-type. On the other hand, the first three peaks in the atomic PDF for pure Ru cores are positioned at distances of 2.67, 3.80, and 4.66 Å, respectively. The distances are very close to the radii of first, second, and third atomic coordination spheres in bulk Ru adopting a hexagonal close packed (hcp)-type structure.³⁹ The observation indicates that the overall atomic structure of pure Ru cores is of a hcp-type. Other experimental studies have also found that the atomic structure of <10 nm pure Pt and Ru particles is fcc- and hcp-type, respectively.^{37,38,40} Inspection of the experimental total PDFs data in Figure 2a also reveals that the thicker the Pt shell of Ru core–Pt shell NPs the closer the resemblance between the respective total PDF and that for pure Pt NPs. The observation indicates that Pt atoms forming the shell are very likely to be arranged in an fcc-type manner. Furthermore, peaks in the total PDF for Pt₇₅Ru₂₅ alloy NPs nearly mirror those in the PDF for pure Pt NPs in terms of position and relative intensity. The observation indicates that the type of atomic arrangement in the former nearly mirrors that in the latter, that is, that the overall atomic arrangement in Pt₇₅Ru₂₅ alloy NPs is of a fcc-type. The total PDF for Pt₃₁Ru₆₉ alloy NPs resembles that for Ru@1Pt NPs having an overall chemical composition of Pt₃₀Ru₇₀. The observation indicates that NPs incorporating somewhat entangled Ru-rich and Pt-rich components, such as the partially segregated alloy-type Pt₃₁Ru₆₉ NPs (see the respective HAADF-STEM image in Figure 1) and NPs composed of distinct Ru core and Pt shell components, such as Ru@1Pt NPs (see the respective HAADF-STEM image in Figure 1), are difficult to tell apart by inspecting experimental total atomic PDFs alone. Studies claiming the opposite should be considered with caution. As shown below, the difficulty disappears when not the total but the respective element specific, that is, differential and partial, atomic PDFs are inspected instead.

To ascertain the foregoing observations, we approached the total PDFs of Figure 2a,b with simplistic models constrained to the 3D periodic fcc- and hcp-type lattices used to describe the atomic structure of bulk Pt and Ru, respectively. The δ -function like peaks in the atomic PDFs derived from the model lattices were broadened by convolution with Gaussian functions as to mimic the usual dynamic (e.g., thermal) and static (e.g., extended NP surface induced) structural disorder in <10 nm metallic particles. At the same time, the model PDFs were multiplied by an artificial function rapidly decaying with real space distances as to mimic the NP finite size. Finally, the unit cell parameters of model lattices were refined so that the model-derived atomic PDFs approached the experimental ones as close as possible. Modeling was done with the help of program PDFgui.⁴¹ Results from the modeling are shown in Figure 2a,b. As shown, a model based on a hcp-type lattice reproduces very well ($R_{\text{wp}} \sim 20\%$) the experimental total PDF for pure Ru cores, confirming that their atomic structure is of a hcp-type. A model based on a fcc-type lattice reproduces very well ($R_{\text{wp}} \sim 19\%$) the total experimental PDF for pure Pt NPs

confirming that their atomic structure is of a fcc-type. A model based on fcc-type lattice reproduces very well ($R_{\text{wp}} \sim 21\%$) the experimental total PDF for Pt₇₅Ru₂₅ alloy NPs confirming that their overall atomic structure is of a fcc-type. The thicker the Pt shell of Ru core–Pt shell NPs, the better a model based on a fcc-type lattice reproduces the respective total PDF (see the trend in R_{wp} values reported in Figure 2a). The result confirms that Pt atoms deposited on Ru cores tend to arrange in an fcc-type manner. Some features of the total PDFs for Pt₃₁Ru₆₉ alloy and Ru@1Pt NPs are reproduced well by a model based on an fcc-type lattice, while other features are reproduced well by a model based on an hcp-type lattice. Neither model, though, can reproduce the respective experimental total PDFs well. The result confirms that both Pt₃₁Ru₆₉ alloy and Ru@1Pt NPs are segregated in Pt-rich and Ru-rich components. However, it also shows that NPs incorporating somewhat entangled Ru-rich and Pt-rich components, such as the partially segregated alloy-type Pt₃₁Ru₆₉ NPs and NPs composed of distinct Ru core and Pt shell components, such as Ru@1Pt (Pt₃₀Ru₇₀) NPs, are difficult to tell apart by crystalline (Bravais-type) lattice constrained modeling alone (see comparable values of respective R_{wp} factors (~ 61 – 65%) in Figure 2a,b). Studies claiming the opposite should be considered with caution. As demonstrated below, 3D modeling going beyond the limits of traditional crystallography and accounting for data from resonant high-energy XRD experiments on the actual NPs studied is much better suited for the job.

As shown in Figure 3a,b, peaks in the Pt-differential and Ru–Ru partial atomic PDFs for all NPs studied here are well-defined. The observation indicates that the arrangement of Ru and Pt species both in the core–shell and alloy NPs, including that at the interfaces inside the NPs, is well-defined and, hence, can be determined unambiguously. In particular, Ru–Ru partial PDFs for Ru@1Pt, Ru@2Pt and Ru@3Pt NPs shown in Figure 3b are practically identical to each other strongly resembling the experimental total PDF for pure Ru cores shown in Figure 2a. Obviously, depositing layers of Pt atoms onto premade Ru cores does not disturb the hcp-type atomic structure of the latter substantially. Recent DFT studies on Ru core–Pt shell NPs have arrived at a similar conclusion.²⁶ On the other hand, data in Figure 3a shows that Pt-differential PDFs for Ru core–Pt shell NPs evolve with the thickness of Pt shell substantially. In particular, peaks in the Pt-differential PDF for Ru@1Pt NPs exhibit a sudden decay at distances longer than 4 Å, i.e. longer than the radius of the second coordination sphere of Pt atoms in the NPs (see the respective step-down-like arrow). Obviously, the number of second, third and more distant neighbors of Pt atoms in Ru@1Pt NPs is reduced greatly as compared, for example, to that of Pt atoms in pure Pt NPs (see the respective PDF shown in Figure 2a).⁴² Such a reduction is to be expected for Pt atoms forming a monolayer enclosing spherical in shape and 3.2 nm in size Ru cores. Peaks in the Pt-differential PDF for Ru@2Pt NPs exhibit a sudden decay at distances longer than 5.5 Å, that is, longer than the radius of the third coordination sphere of Pt atoms in the NPs (see the respective arrow). Obviously, the number of third, fourth, and more distant neighbors of Pt atoms in Ru@2Pt NPs is reduced greatly as compared, for example, to that of Pt atoms in pure Pt NPs. Such a reduction is to be expected for Pt atoms forming a bilayer enclosing spherical in shape and 3.2 nm in size Ru cores. Peaks in the Pt-differential PDF for Ru@3Pt NPs exhibit a sudden decay at distances longer than 6–7 Å, that is, longer than the radius of the fifth to sixth coordination sphere of Pt

atoms in the NPs (see the respective arrow). Obviously, the number of fifth, sixth, and more distant neighbors of Pt atoms in Ru@3Pt NPs is reduced greatly as compared, for example, to that of Pt atoms in pure Pt NPs. Such a reduction is to be expected for Pt atoms forming a stack of 3 layers enclosing spherical in shape and 3.2 nm in size Ru cores. A closer look at the data in Figure 3a shows that, although they exhibit a sudden decay at different real-space distances, peaks in Pt-differential PDFs for Ru@1Pt, Ru@2Pt and Ru@3Pt NPs are similar to each other with respect to position and relative intensity. Furthermore, peaks in Pt-differential PDFs for Ru@1Pt, Ru@2Pt, and Ru@3Pt NPs appear similar to those in the total PDF for pure Pt NPs exhibiting, as confirmed by the results of crystalline-lattice constrained modeling (Figure 2a), an fcc-type structure. Obviously, as predesired, Ru@1Pt, Ru@2Pt, and Ru@3Pt NPs studied here consist of virtually identical hcp-type Ru cores and distinctive fcc-type Pt shells made of one, two, and three atomic layers, respectively. Therefore, the Ru core–Pt shell interface in these NPs can be described as heterogeneous in a sense that it is between NP components of completely different both chemical composition and atomic-scale structure.

Also shown in Figure 3a, peaks in Pt-differential PDFs for Pt₃₁Ru₆₉ and Pt₇₅Ru₂₅ alloy type NPs decay just about linearly and not stepwise with interatomic distances (see the respective straight lines). This is to be expected, considering that Pt atoms in Pt–Ru alloy type NPs are distributed within spherical particles while Pt atoms in Ru core–Pt shell NPs occupy thin shells enveloping spherical Ru cores. Though decaying at different rates,⁴³ peaks in the Pt-differential PDF for Pt₃₁Ru₆₉ and those in the Pt-differential for Pt₇₅Ru₂₅ alloy NPs are similar to each other in terms of position and relative intensity. Peaks in the Pt-differential PDFs for Pt₃₁Ru₆₉ and Pt₇₅Ru₂₅ alloy NPs also appear similar to those in the PDF for pure Pt NPs exhibiting a fcc-type structure. On the other hand, data in Figure 3b shows that Ru–Ru partial PDF for Pt₃₁Ru₆₉ and that for Pt₇₅Ru₂₅ alloy NPs differ substantially. In particular, Ru–Ru PDF for Pt₃₁Ru₆₉ alloy NPs resembles that for pure Ru cores shown in Figure 2a. By contrast, Ru–Ru PDF for Pt₇₅Ru₂₅ alloy NPs resembles that for pure Pt NPs shown in Figure 2a. Obviously, Ru atoms in Ru-rich Pt₃₁Ru₆₉ alloy type NPs arrange in an hcp-type manner maintaining the type of atomic arrangement in bulk Ru, whereas Ru atoms in Ru-poor Pt₇₅Ru₂₅ alloy type NPs arrange in an fcc-type manner adopting the arrangement of majority Pt atoms in these NPs. Therefore, the interface between Pt-rich and Ru-rich components of partially segregated Pt₃₁Ru₆₉ alloy NPs can be described as a largely heterogeneous (see the respective HAADF image in Figure 1) in a sense that it is between NP components of largely different both chemistry and atomic-scale structure (see the different shape of the respective Pt-differential and Ru–Ru partial atomic PDFs shown in Figure 3a,b). The interface(s) inside Pt₇₅Ru₂₅ alloy type NPs, if any, can be described as largely homogeneous because Pt and Ru species in the NPs are not only well intermixed together (see the respective HAADF-STEM image in Figure 1) but are also arranged in the same fcc-type manner (see the similar shape of respective Pt-differential and Ru–Ru partial PDFs shown in Figure 3a,b).⁴⁴

Furthermore, as can be seen in Figure 3a, Pt-differential PDF for partially segregated Pt₃₁Ru₆₉ alloy NPs and that for Ru@1Pt NPs (Pt₃Ru₇₀) are rather different. Pt-differential PDF for single phase Pt₇₅Ru₂₅ alloy NPs and those for Ru core–Pt shell NPs are also different. Evidently, alloy type NPs, such as

partially segregated Pt₃₁Ru₆₉ and single-phase Pt₇₅Ru₂₅, and NPs composed of distinct Ru core and Pt shell components, such as Ru@1Pt (Pt₃₀Ru₇₀), Ru@2Pt (Pt₄₆Ru₅₄) and Ru@3Pt (Pt₆₀Ru₄₀) NPs, can be differentiated clearly by inspecting the respective element specific atomic PDFs alone. The type of atomic structure in the different components of composite NPs, in particular the hcp-type structure of Ru cores and fcc-type structure of Pt shells in Ru core–Pt shell NPs, as well as particular morphological characteristics of the components, such as the number of atomic layers forming Pt shell in the Ru core–Pt shell NPs, can also be determined precisely by inspecting the respective element-specific atomic PDFs alone. The type of interfaces inside composite NPs (e.g. completely heterogeneous in Ru core–Pt shell NPs vs largely homogeneous in alloy-type Pt₇₅Ru₂₅ NPs) can also be determined precisely by inspecting element specific atomic PDFs alone, i.e. without the help of 3D structure modeling and/or evoking theoretical predictions. This can be very valuable to large-scale, e.g. industrial, production of composite NPs since both the structure type of NP components and the type of interfaces between the NP components will be possible to be monitored by experiment alone and the fabrication process adjusted accordingly.

To reveal the exact 3D arrangement of Ru and Pt species at the core/shell interface inside Ru@1Pt, Ru@2Pt and Ru@3Pt NPs we built 3D models for the NPs using the respective total and element specific PDFs as a guide. For the sake of comparison, we also built 3D models for Pt–Ru alloy-type NPs. Models featured atomic configurations with the chemical composition, size, and shape of actual NPs studied as determined by ICP-AES and HR-TEM experiments, respectively. Modeling was done by hybrid reverse Monte Carlo (RMC) simulations under nonperiodic boundary conditions. In the simulations, the positions of atoms in the structure models were adjusted, including switching the positions of nearby unlike atoms, so that the difference between the model-derived and experimental total and element specific PDFs is minimized. At the same time, model's energy was also minimized, that is, the model's stability was maximized, using pairwise potentials of Lennard–Jones type. More details of the hybrid RMC simulations are given in the Methods section of the [Supporting Information](#).

As a first step, a 3D model for pure Ru cores was built. The initial atomic configuration featured a piece of crystalline hcp Ru 3.2 nm in size and spherical in shape. The configuration made sense considering the results of crystalline lattices constrained modeling shown in Figure 2a. The configuration was refined independently against the experimental total PDF for pure Ru cores and Ru–Ru partial PDFs for Ru@1Pt, Ru@2Pt and Ru@3Pt NPs. The resultant four independent models reproduced the respective experimental PDF data very well. Analysis of the RMC refined models in terms of Ru–Ru atomic pair distances, coordination numbers (CNs) and Ru–Ru–Ru bond angles distribution (Figure S5d) showed that the models are virtually identical. This did not come as a surprise considering the great similarity between the respective experimental PDFs. Therefore, for the sake of efficiency, one of the models for Ru cores was used in the RMC simulations of all Ru core–Pt shell NPs. The model is shown in Figure 4 (top).

A 3D model for Ru@1Pt NPs was generated by positioning Pt atoms on the surface of the 3D model for Ru cores so that the atoms both packed densely in a monolayer and the overall

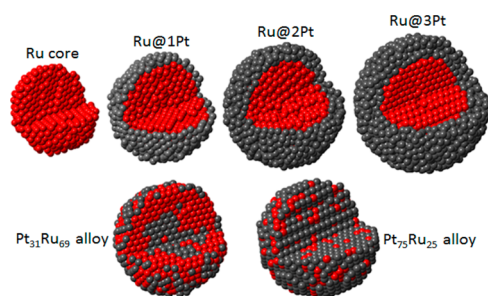


Figure 4. (Top) 3D structure models for (left to right) pure Ru cores, Ru@1Pt, Ru@2Pt, and Ru@3Pt core-shell NPs. Atomic layers at the core/shell interface in the models are stacked in a Ru(BAB)\Pt(C)-, Ru(BAB)\Pt(CA)-, and Ru(BAB)\Pt(CAB)-type sequence, respectively. (Bottom) 3D structure models for (left) Pt₃₁Ru₆₉ and (right) Pt₇₅Ru₂₅ alloy type NPs. Pt and Ru atoms in the latter are well intermixed together forming a homogeneous fcc-type alloy. Pt and Ru atoms in the former segregate, rendering the NPs “onion-like”. Ru atoms are in red, and Pt atoms are in dark gray. Note, the 3D models for the core-shell NPs are not perfectly spherical in shape. For example, the cross section of the 3D model for Ru@2Pt NPs may be viewed as an irregular ellipse with a minor and major axis of 4.35 and 4.6 nm, respectively. One reason for the 3D models not to be perfectly spherical is that the models feature hcp Ru cores and fcc Pt shells, wherein atoms are as densely packed as possible and meet a strict Pt:Ru relative ratio as determined by ICP-AES. Noteworthy, independent SAXS experiments have also indicated that Ru core-Pt shell NPs of the type studied here are not necessarily perfect spheres in shape.⁷²

model’s composition, that is, the relative Pt/Ru ratio, corresponded to that (Pt₃₀Ru₇₀) determined by ICP-AES. At the same time, positions of Pt atoms within the layer and of Ru atoms in the core beneath it were adjusted so that the difference between the model-derived and respective experimental total, Pt-differential and Ru-Ru partial atomic PDFs is reduced as much as possible. A fragment of a model featuring Pt monolayer conforming to the hcp(BAB)-type stacking sequence of atomic layers in Ru core, that is, featuring a Ru(BAB)\Pt(A)-type interface, is shown in Figure 5a. A fragment of a model featuring Pt monolayer not conforming to the hcp(BAB)-type stacking sequence of atomic layers in Ru core but to the fcc(ABC)-type one occurring in fcc Pt, that is, featuring a Ru(BAB)\Pt(C)-type interface, is shown in Figure 5b.³⁹ Total and element specific atomic PDFs derived from the models are shown in Figures 2 and 3. As data in Figure 3b,c shows, and as it can be expected, both models reproduce the respective experimental Ru-Ru PDF in very good detail. The 3D model featuring an interface of Ru(BAB)\Pt(A) type, however, clearly fails in reproducing the experimental Pt-differential PDF for Ru@1Pt NPs in the region of interatomic distances longer than 4 Å, that is, longer than the radius of the second coordination of Pt atoms (Figure 3c). The model does not reproduce well the experimental total PDF data either (Figure 3c). Though, here, the disagreement between the model-derived and experimental data is less obvious because total PDFs reflect Ru-Ru, Pt-Ru, and Pt-Pt atomic pairs all together, whereas Pt-differential ones reflect Pt-Pt and Pt-Ru atomic pairs only. On the other hand, the 3D model featuring an interface of Ru(BAB)\Pt(C) type, shown in Figure 4 (top row), reproduces the respective experimental total (Figure 2c) and element specific (Figure 3a,b) PDFs in very good detail revealing how indeed Ru and Pt species at the core/shell interface inside Ru@1Pt NPs arrange in 3D space. Evidently,

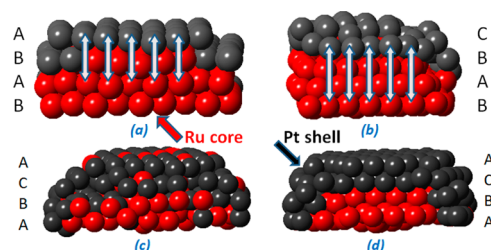


Figure 5. Fragments from 3D models of Ru core-Pt shell NPs featuring different types of stacking of the atomic layers at the core/shell interface. (a) Fragment from 3D model for Ru@1Pt NPs wherein atomic layers at the core/shell interface are stacked according to the hcp(BABA)-type sequence of atomic layers in bulk Ru. (b) Fragment from 3D model for Ru@1Pt NPs wherein atomic layers at the core/shell interface are stacked according to the fcc(ABC)-type sequence of atomic layers in bulk Pt. (c) Fragment from 3D model of Ru@2Pt NPs, wherein 25% of Pt atoms from the shell and a respective number of Ru atoms from the top two layers of the core have had their positions interchanged as to mimic a partial alloying of Pt and Ru species at the core/Pt shell interface. (d) Fragment of 3D model of Ru@2Pt NPs wherein the hcp Ru core and fcc Pt shell are completely segregated. Ru atoms are in red, and Pt atoms are in dark gray. Note, here, both fcc- and hcp-type structures are considered in terms of closely packed layers of atoms. The difference between the fcc- and hcp-type structure is the stacking sequence of atomic layers. The hcp-type stacked layers cycle among two positions (BABA), whereas the fcc-type stacked layers cycle between three positions (ABC). Notice how atoms of the third layer in the hcp-type structure (follow the vertical arrows in 5a) are in exactly the same position as the atoms in the first layer. On the other hand, atoms of the third and first layers in the fcc-type structure (follow the vertical arrows in panel b) are not aligned.

3D modeling guided by total and element-specific atomic PDFs can reveal the 3D atomic arrangement at interfaces inside NPs in fine detail even when one of the NP components involved in the interfaces is an atomic monolayer alone. Note, other element-specific techniques such as, for example, EXAFS may encounter difficulties in differentiating between interfaces of the Ru(BAB)\Pt(A) and Ru(BAB)\Pt(C) type because the first and second neighbor Ru-Ru, Pt-Ru, and Pt-Pt atomic pair distances and coordination numbers for these interfaces are essentially the same.

A 3D model for Ru@2Pt NPs was generated by positioning Pt atoms on the surface of the 3D model for Ru cores so that the atoms both packed densely forming two distinct layers and the overall model’s composition, i.e. the relative Pt/Ru ratio, corresponded to that (Pt₄₆Ru₅₄) determined by ICP-AES. At the same time positions of Pt atoms within the layers and of Ru atoms in the core beneath the layers were adjusted so that the difference between the model-derived and respective experimental total, Pt-differential and Ru-Ru partial atomic PDFs is reduced as much as possible. Several stacking sequences of Ru and Pt layers at the Ru core/Pt shell interface were attempted, and the Ru(BAB)\Pt(CA) one emerged best. The respective 3D model is shown in Figure 4 (first row). A fragment of the model, exposing the Ru(BAB)\Pt(CA) type interface, is shown in Figure 5d. The very good agreement between that model-derived and respective experimental total and element specific atomic PDFs is documented in Figures 2c and 3a,b.

A 3D model for Ru@3Pt NPs was generated by positioning Pt atoms on the surface of the 3D model for Ru cores so that the atoms both packed densely forming three distinct layers and the overall model composition, that is, the relative Pt/Ru ratio,

corresponded to that ($\text{Pt}_{60}\text{Ru}_{40}$) determined by ICP-AES. At the same time, positions of Pt atoms within the layers and Ru atoms in the core beneath the layers were adjusted so that the difference between the model-derived and respective experimental total, Pt-differential, and Ru–Ru partial atomic PDFs is reduced as much as possible. Several stacking sequences of Ru and Pt layers at the core/shell interface were tested, and the Ru(BAB)\Pt(CAB) one was found to reproduce the experimental data best. The respective 3D model is shown in Figure 4 (first row). The very good level of agreement between that model-derived and respective experimental total and element specific PDFs is documented in Figures 2c and 3a,b.

Note, in the course of hybrid RMC simulations, 3D models featuring intermixing of Pt and Ru species at the Ru core/Pt shell interface were also attempted but discarded because they failed in reproducing the experimental element specific PDFs in good detail. An example of such a model is shown in Figure 5c. Its failure to reproduce the experimental PDF data is documented in Figure 3d. The example testifies to the capability of element-specific atomic PDFs to accurately reveal the mutual distribution of distinct atomic species at interfaces inside NPs. In light of our findings, the interface between the Ru core and Pt shell in Ru@1Pt, Ru@2Pt, and Ru@3Pt NPs studied here can be described as a sharp and completely heterogeneous one in a sense that both the type of atomic species (Ru vs Pt) and the type of arrangement of the distinct atomic species (hcp vs fcc) at the interface change abruptly. The hcp-type arrangement of atoms in the Ru core and the fcc-type arrangement of atoms forming the Pt shell in Ru@1Pt, Ru@2Pt, and Ru@3Pt NPs is well illustrated by the distribution of Ru–Ru–Ru and Pt–Pt–Pt bond angles extracted from the respective 3D models, as data in Figure S5 show.

Initial models for Pt–Ru alloy type NPs featured spherical configurations of about 3000 Pt and Ru atoms densely packed in proportions consistent with the chemical composition of actual $\text{Pt}_{31}\text{Ru}_{69}$ and $\text{Pt}_{75}\text{Ru}_{25}$ alloy NPs studied here, as determined by ICP-AES. The configurations were refined against the respective experimental total and element-specific atomic PDFs by hybrid RMC simulations. The ability to switch positions of nearby unlike atoms, that is, let atoms diffuse through the model atomic configurations, implemented in hybrid RMC (see the Methods section of the Supporting Information) was vital for converging to 3D models reproducing the experimental data in very good detail. So-built models for Pt–Ru alloy NPs are shown in Figure 4 (bottom row). The very good agreement between the model-derived and experimental PDFs is documented in Figures 2d and 3a,b. Analysis of the model for $\text{Pt}_{75}\text{Ru}_{25}$ alloy type NPs in terms of Pt–Pt–Pt, Ru–Ru–Ru, Pt–Ru–Pt, and Pt–Ru–Ru bond angles (Figures S5 and S6a) and distribution of Pt atoms across the model (Figure S7a) confirmed that Ru and Pt species in the NPs are both very uniformly intermixed together and fcc-type arranged. The result substantiates a conclusion that, within the limits of experimental accuracy, $\text{Pt}_{75}\text{Ru}_{25}$ alloy type NPs studied here can be considered virtually free of internal interfaces. On the other hand, a closer look at the 3D model for partially segregated $\text{Pt}_{31}\text{Ru}_{69}$ alloy type NPs (Figure 4, bottom row) and the distribution of Pt atoms in it (Figure S7b) show that, indeed, the NPs are onion-like, and they belong to a class of composite NPs that is also extensively pursued nowadays. In particular, per the results of 3D modeling, partially segregated $\text{Pt}_{31}\text{Ru}_{69}$ alloy-type NPs may be

considered as composed of three components: top surface rich in Pt species, a cluster of Pt atoms at the NP center and a thick subsurface band of Ru atoms.⁴⁵ Analysis of the 3D model for $\text{Pt}_{31}\text{Ru}_{69}$ alloy NPs in terms of Pt–Pt–Pt, Ru–Ru–Ru, Ru–Pt–Ru, and Pt–Pt–Ru bond angle distributions (Figures S5 and S6b) confirms that Pt and Ru species in the NPs are largely fcc- and hcp-type arranged, respectively. The result substantiate a conclusion that the interfaces between the three components of onion-like $\text{Pt}_{31}\text{Ru}_{69}$ NPs can be described as smooth and largely heterogeneous in a sense that the change in the type of atomic species and the type of atomic arrangement at the interfaces change gradually resembling one cycle of a sine wave (Figure S7b). Note, onion-like NPs would be difficult to characterize by imaging techniques sensitive to the chemical type of atomic species such as HAADF-STEM because HAADF-STEM images, like any other images, are merely a projection down an axis. Element-specific spectroscopy techniques such as, EXAFS, energy-dispersive X-ray spectroscopy (EDX), and others, may also have difficulties in characterizing onion-like NPs because, due to their nature, such techniques would yield data averaged out across the NPs (e.g., see ref 27).

Here, it is worth noting that, for the sake of efficiency, the starting configurations used in the 3D modeling of Ru core–Pt shell and Pt–Ru alloy NPs were not selected at random. On the contrary, atomic configurations consistent with (1) the size, shape and chemistry of the NPs studied, as determined by HR-TEM and ICP-AIS, respectively; (2) the results of crystalline lattices constrained modeling presented in Figure 2a; and (3) characteristic features of the respective total and element specific atomic PDF, such as the position, intensity and rate of decay of the PDF peaks, were considered as starting ones only. For example, the modeling of Ru core–Pt shell NPs featured depositing of Pt atoms on the same hcp Ru core so that the atoms formed distinct and closely packed layers. The former was suggested by the fact that the experimental Ru–Ru PDFs for the core–shell NPs and the experimental PDF for hcp Ru cores appeared virtually identical (Figure 2b). The latter took into account the stepwise decay of the respective Pt-differential PDFs (Figure 3a). On the other hand, the starting model for $\text{Pt}_{75}\text{Ru}_{25}$ alloy type NPs featured an atomic configuration with an overall fcc-type structure suggested by the results of crystalline lattices constrained modeling and the similarity between Pt-differential and Ru–Ru partial PDFs for the NPs on one side and that for pure Pt NPs on the other. Indeed justified, reducing the space of possible starting atomic configurations to be explored to improve the efficiency of 3D modeling of metallic NPs is not a novelty. It has been practiced with success for quite some time.^{46–48}

With realistic 3D models at hand, all important structural characteristics of interfaces inside NPs can be derived precisely and used for assessing the influence of the former on the functionality of the latter. Here, we concentrate on the structural characteristics of core/shell interface relevant to the activity and stability of Ru core–Pt shell NPs as catalysts in fuel cells. In particular, we derive Pt–Pt bonding distances near the interface and the evolution of these distances with the thickness of Pt shell. The reason is as follows: Several studies have claimed that the improvement in the catalytic functionality of Ru core–Pt shell NPs, as compared to that of pure Pt NPs, is due largely to bonding (heterometallic) interactions between Ru and Pt atoms at the core/shell interface, often referred to as a ligand effect, and changes in the distances between Pt atoms

near the core/shell interface, often referred to as a strain effect.^{25,26,29,49–54} Change in the Pt-to-Pt metal bond length, often referred to as size of Pt atoms, and, hence, in all Pt–Pt atomic pair distances near the Ru core/Pt shell interface may be expected because, for the atomic-level stresses at the interface to be optimized, the larger in size Pt atoms (2.77 Å) should contract and the smaller in size Ru atoms (2.67 Å) should expand as that the ratio of their size becomes as close to one as possible.^{52–54} Coupling between *d* orbitals of Pt and Ru species facing each other at the core/shell interface, that is, emerging of Pt–Ru bonding interactions across the core/shell interface, may be expected too.^{50–57} The specific claim is that, acting in sync, the likely heterometallic interactions and optimization of atomic-level stresses, that is, contraction of Pt atoms taking place at the Ru core/Pt shell interface modify the electronic structure of Pt atoms near the interface. The modification is such that *d* electron states of Pt atoms shift down in energy which, in turn, reduces the strength of interaction between chemical species, including CO, and the surface of Ru core–Pt shell NPs facilitating critical steps of gas-phase oxidation of CO and electro-oxidation of alcohols.^{49–54,58} However, the interplay between the heterometallic interactions and optimization of atomic-level stresses, both arising at the sharp interface between the chemically and structurally distinct core and shell components of Ru core–Pt shell NPs, is still unclear. As shown below, precise knowledge of Pt–Pt bonding distances in Ru@1Pt, Ru@2Pt and Ru@3Pt NPs, obtained by resonant high-energy XRD coupled to element-specific PDFs analysis, can help resolve this ambiguity.

Distribution of Pt-to-Pt metal bond lengths in Ru@1Pt, Ru@2Pt, and Ru@3Pt NPs, wherein the Ru core/Pt shell interface is of the Ru(BAB)\Pt(C), Ru(BAB)\Pt(CA), and Ru(BAB)\Pt(CAB) type, respectively, is shown in Figure S8a. For comparison, distribution of Pt-to-Pt metal bond lengths in “onion-like” Pt₃₁Ru₆₉ and homogeneous Pt₇₅Ru₂₅ alloy NPs is shown in Figure S8b. The distributions are derived from the respective 3D models shown in Figure 4. As data in Figure S8a shows, on average, Pt-to-Pt metal bond length in Ru@1Pt NPs is 2.72 Å, that is, contracted by about 1.8% as compared to the average Pt-to-Pt metal bond length of 2.77 Å in bulk Pt.³⁹ The average Pt-to-Pt metal bond length in Ru@2Pt NPs is 2.74 Å indicating that depositing a second Pt layer on the Ru cores reduces the compressive strain within the NP shell to about 1.1%. The average Pt-to-Pt metal bond length in Ru@3Pt NPs is 2.76 Å, that is, contracted by about 0.4% as compared to that in bulk Pt.³⁹ The finding indicates that a Pt shell of 3 atomic layers is barely compressed. Analysis of the distribution of Pt-to-Ru metal bond lengths in Ru@1Pt, Ru@2Pt and Ru@3Pt NPs showed a similar pattern (Figure S9), namely, that Pt-to-Ru metal bond length in Ru core–Pt NPs is somewhat contracted, as compared to that in “onion-like” Pt₃₁Ru₆₉ and homogeneous Pt₇₅Ru₂₅ alloy NPs, and the degree of this contraction diminishes (by about 0.3%) with the thickness of Pt shell.

According Pauling’s theory of chemical bonds and as confirmed by experiments the metal-to-metal bond length, strength and the electronic structure of metallic species involved are intimately coupled.^{55–57} Therefore, changes in Pt–Pt bonding distances in Ru core–Pt shell NPs would indicate concurrent changes in the electronic structure of Pt atoms forming the NP shell and vice versa. Then, considering our findings and the findings of others,^{49,53,58} it may be conjectured that Ru@1Pt NPs would clearly outperform Ru@

2Pt, Ru@3Pt and pure Pt NPs as catalysts for the aforementioned reactions. It may also be conjectured that Ru@2Pt and, to a certain extent, Ru@3Pt would be better catalysts than pure Pt NPs. Furthermore, considering data for Pt–Pt bond distances in onion-like Pt₃₁Ru₆₉ and homogeneous Pt₇₅Ru₂₅ alloy NPs presented in Figure S8b it may be conjectured that Ru@1Pt NPs would outperform Pt–Ru alloy NPs as catalysts at the anode of fuel cell though the so-called “bifunctional mechanism” may become operative in the latter. For reference, the bifunctional mechanism envisages that Pt and Ru species intermixed at the surface of Pt–Ru alloy NPs do not interact but act cooperatively as to promote particular steps of chemical reactions taking place at the anode of fuel cells.^{31,32} This may or may not be the case with Ru@2Pt and, in particular, Ru@3Pt NPs, wherein the contraction of Pt–Pt bonding distances is a fraction of that exhibited by Ru@1Pt NPs.

To cross check the conjectures of our purely atomic-scale structure study, we evaluated the performance of NPs of the type studied here as catalysts for electrooxidation of methanol using cyclic voltammetry (CV) analysis. Details of the analysis can be found in ref 29. Exemplary CV curves are shown in Figure S10. We found that Ru@1Pt NPs exhibited 3.2-fold improvement in CO-tolerance and 2.4-fold enhancement in the current output at a standard for direct methanol fuel cells operating potential of 300 mV (vs the Ag/AgCl reference electrode used in the cell) as compared to pure Pt NPs. With Ru@3Pt NPs the improvement in CO-tolerance and current output was found to be, respectively, 1.4-fold and 1.3-fold only. When measured under similar conditions, onion-like Pt₃₁Ru₆₉ and homogeneous Pt₇₅Ru₂₅ alloy NPs exhibited a marginal improvement as catalysts for electrooxidation of methanol as compared to pure Pt NPs. It has been repeatedly shown that the performance of binary metal NP catalysts, including core–shell and alloy type ones, also depends on details in the NP preparation, the amount of NP catalyst loaded on the fuel cell anode, type of reference Pt NPs used, and others.^{59–63} Therefore, we refrain from comparing the improvement in CO-tolerance and current output reported above with those reported by others. We would like to point out, however, that the findings of our catalytic study, in particular that Pt–Ru NPs studied here can be ranked as Ru@1Pt > Ru@2Pt > Ru@3Pt > Pt–Ru alloy > Pt NPs with regard to their performance as catalysts in fuel cells, are very much in line with the findings of catalytic studies of others.^{25–27,51,52,64} Altogether, the findings of our resonant high-energy XRD and element specific PDFs study, as corroborated by the findings of our independent catalytic study, indicate that 2% to 0.4% contraction of Pt–Pt bonding distances, accompanied by a smaller yet clearly identifiable (~0.3%) contraction of Ru–Pt bonding distances, may alone suffice to explain the promotional effect of core/shell interface on the catalytic functionality of NPs composed of an hcp Ru core and fcc Pt shell that is one to three atomic layers thick, respectively.

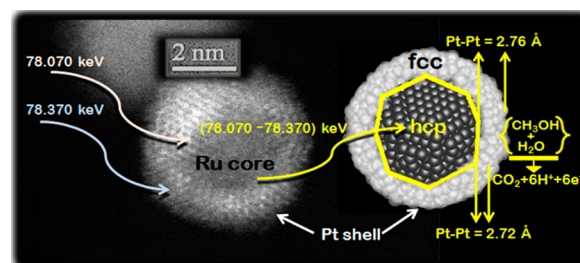
Some DFT studies, however, have argued not only that both the strain and ligand effects contribute to the increased catalytic functionality of Ru core–Pt shell NPs but also that these effects can be isolated and evaluated independently. In particular, DFT studies featuring epitaxial layers of (hcp-type !) Pt grown on the (0001) atomic plane of perfect hcp Ru crystals have argued that the core/shell interface induced strain and ligand effects would be of equal importance to the catalytic functionality of Ru core–Pt shell NPs as far as the Pt shell is up to four atomic

layers thick.^{50,65} The studies have also argued that the ligand effect would become insignificant whereas the strain effect, that is, the contraction of Pt–Pt bonding distances, remain substantial for Ru core–Pt shell NPs wherein the Pt shell is up to 10 atomic layers thick. As we show here this may not necessarily be the case with actual, not computer-generated, NPs made of a thin (fcc-type !) Pt shell deposited on the definitely not perfect-crystal-like surface of 3.2 nm in size and spherical in shape hcp-type Ru cores. The disagreement between the present and aforementioned DFT studies may not come as a surprise because it has long been recognized that conclusions drawn from simple model systems, such as planar-type interfaces between 3D perfectly periodic Pt layers and bulk-like Ru substrate, can be useful but not accurate enough when applied to more realistic and so complex systems, such as the Ru core\Pt shell interface inside less than 10 nm in size and spherical in shape NPs.⁶⁶ In our view, the accuracy of theory for interfaces inside NPs can be improved by employing model systems that are more realistic than the ones currently used. For example, more realistic model systems may be based on segments of the curved and rugged (see the non-negligible spread of Pt–Pt bonding distances shown in Figure S8a) Ru core\Pt shell interfaces, which have been excised from 3D models, tested, and refined against experimental total and element-specific atomic PDFs. The usefulness of such an approach was demonstrated in our recent work exploring Ru NPs as catalysts for the technologically important Fischer–Tropsch reaction used to convert syngas (a mixture of H₂ and CO) into clean and cheap liquid fuels.⁶⁷ In particular, two atomic layer thick slabs (~150 atoms each) were excised from the top surface of hybrid RMC-refined models for 1.2, 3.4, 3.7, and 5.2 nm Ru particles. The segments were optimized further by DFT, and the energy barriers for CO dissociation at particular sites on the slab top surface were computed. The latter allowed assessing the rate of Fischer–Tropsch reaction as a function of the size of Ru NPs on a sound and not assumed structural basis.⁶⁸

First, CNs for Pt atoms forming the very top layer of Ru@2Pt and Ru@3Pt NPs were also derived from the respective 3D models. The reason was that the local coordination of Pt surface atoms in Ru core–Pt shell NPs has been suggested as a tunable parameter for improving particle's catalytic functionality for yet another technologically important reaction, in particular oxygen reduction reaction (ORR).⁶⁹ The reaction takes place at the cathode of fuel cells and in metal-air batteries.^{70,71} In particular, it has been suggested that by maximizing the number of Pt surface atoms with a given local coordination, that is, by making use of the so-called atomic ensemble effect⁵³ and, at the same time, properly tuning up the Ru core\Pt shell interface the strength of interaction between oxygen species and the top surface of Ru core–Pt shell NPs can be modified in a way promoting ORR.⁶⁹ The CNs are shown in Figure S8c; most Pt surface atoms in Ru@2Pt NPs are 8, 7, 6, and 5-fold coordinated and occupy sites within close-packed, planar-type atomic configurations, at terraces, edges, and corners at the NP surface, respectively. Depositing a third Pt layer on Ru cores almost doubles the number of Pt surface atoms sitting at terraces, mostly at the expense of Pt surface atoms sitting at edges and corners. DFT has predicted that Ru@2Pt NPs wherein Pt surface atoms exceedingly occupy corner- and edge-type sites and Ru@3Pt NPs wherein Pt surface atoms exceedingly occupy terrace-type sites would exhibit an improved catalytic functionality for ORR. Prelimi-

nary experiments have confirmed the feasibility of DFT predictions. Evidently, resonant high-energy XRD coupled to element specific atomic PDFs analysis can be invaluable to exploring core–shell NPs for practical applications by providing precise atomic-level knowledge both of the core\shell interface inside the NPs and of the NP surface, as illustrated in Scheme 1.

Scheme 1. Precise Determination of the 3D Atomic Arrangement at Functional Interfaces Inside Composite NPs by Resonant High-Energy XRD Coupled to Element Specific Atomic PDFs Analysis⁴⁴



“The example features the core\shell interface in Ru core–Pt shell NPs (HAADF-STEM image at the center) used as catalysts in fuel cells, including for electrooxidation of methanol (CH₃OH) as shown on the right part of the scheme. In particular, two diffraction patterns are collected using X-rays with energy of 78.070 and 78.370 keV which are, respectively, 325 and 25 eV below the K adsorption edge (78.395 keV) of Pt atoms. The pattern obtained using X-rays with higher energy is subtracted from the one obtained using X-rays with lower energy. The difference of intensity is entirely due to the difference between the dispersion corrections to the atomic X-ray scattering factor of Pt atoms. Accordingly, the Fourier transform of difference intensity, the so-called Pt-differential atomic PDF, reflects atomic correlations specific to Pt atoms, including Pt–Pt bonding distances at the Ru core–Pt shell interface (see the vertical arrows). The evolution of these distances with the thickness of Pt shell can help achieve a better understanding of the influence of the interface on the catalytic functionality of Ru core–Pt shell NPs and, hence, gain more control over using the former for improving the latter.

4. CONCLUSION

Advancing science and technology will keep searching for NPs with added functionality by interfacing chemically or structurally distinct entities into composite NPs. The entities or interfaces explored may not necessarily have bulk analogues or be possible to predict from first principles. This research effort can only benefit from advanced analytical techniques such as resonant high-energy XRD coupled to element-specific atomic PDFs analysis that, as demonstrated here, can provide precise knowledge of the 3D atomic arrangement across composite NPs, including at the interface(s) they comprise. The knowledge can help us better understand the relationship between the interface(s) and NP functionality and, hence, enable a rational design approach to utilizing the former for improving the latter. Also, it can provide a sound basis for testing and improving the accuracy of theory of interfaces inside NPs and so help unlock its predictive power. The technique succeeds by virtue of its high spatial resolution, inherent element specificity, and applicability to NPs of any size, shape, or atomic-scale structure.

In particular, the high spatial resolution comes through using high-energy X-rays for probing the higher energy K absorption

edges of atomic species in NPs. The inherent element specificity is due to the substantially different energy of the K absorption edges of distinct atomic species. The applicability to NPs, including their components, of any size, shape, and atomic-scale structure is due to the atomic PDFs taking into account both the Bragg-like and non-negligible diffuse component of high-energy XRD patterns of NPs. Besides, atomic PDF analysis does not imply any periodicity. The technique is noninvasive and can reveal the true nature of interfaces inside NPs, even if some of the NP components involved in the interfaces are a single atomic layer thick. Furthermore, it requires a small amount of NPs as loaded on solid supports or dispersed in solutions, enabling in situ studies when necessary. Last but not least, thanks to the rapidly increasing number of synchrotron sources of high-energy X-rays, it is becoming more widely accessible worldwide. As such, the technique has all the potential needed to become an indispensable research tool for science and technology of internal interfaces in discrete materials confined to nanoscale dimensions.

■ ASSOCIATED CONTENT

Supporting Information

The Supporting Information is available free of charge on the ACS Publications website at DOI: 10.1021/acsami.5b07391.

Experimental and computational methods, TEM images, and additional figures. (PDF)

■ AUTHOR INFORMATION

Corresponding Author

* E-mail: petko1vg@cmich.edu.

Notes

The authors declare no competing financial interest.

■ ACKNOWLEDGMENTS

Work for this study was supported by DOE-BES Grant DE-SC0006877. Work at the Advanced Photon Source was supported by DOE under Contract DEAC02-06CH11357. Thanks are due to the group of Prof. C.J. Zhong from SUNY, Binghamton, for providing Pt–Ru alloy NPs.

■ REFERENCES

- (1) Gerberich, W. W.; Mook, W. M.; Perrey, C. R.; Carter, C. B.; Baskes, M. I.; Mukherjee, R.; Gidwani, A.; Heberlein, J.; McMurry, P. H.; Girshick, S. L. Superhard Silicon Nanospheres. *J. Mech. Phys. Solids* **2003**, *51*, 979–992.
- (2) Haruta, M. Size- and Support-dependency in the Catalysis of Gold. *Catal. Today* **1997**, *36*, 153–166.
- (3) Cortie, M. B.; McDonagh, A. M. Synthesis and Optical Properties of Hybrid and Alloy Plasmonic Nanoparticles. *Chem. Rev.* **2011**, *111*, 3713–3735.
- (4) Carbone, L.; Cozzoli, P. D. Colloidal Heterostructured Nanocrystals: Synthesis and Growth Mechanisms. *Nano Today* **2010**, *5*, 449–493.
- (5) Howes, P. D.; Chandrawati, R.; Stevens, M. M. Colloidal Nanoparticles as Advanced Biological Sensors. *Science* **2014**, *346*, 1247390–10.
- (6) Wei, S.; Wang, Q.; Zhu, J.; Sun, L.; Lin, H.; Guo, Zh. Multifunctional Composite Core-Shell Nanoparticles. *Nanoscale* **2011**, *3*, 4474–4502.
- (7) Ji, B.; Giovanelli, E.; Habert, B.; Spinicelli, P.; Nasilowski, M.; Xu, X.; Lequeux, N.; Hugonin, J.-P.; Marquier, F.; Greffet, J.-J.; Dubertret, B. Non-blinking Quantum Dot with a Plasmonic Nanoshell Resonator. *Nat. Nanotechnol.* **2015**, *10*, 170–175.
- (8) Hirakawa, T.; Kamat, P. V. Charge Separation and Catalytic Activity of Ag@TiO₂ Core-Shell Composite Clusters under UV-Irradiation. *J. Am. Chem. Soc.* **2005**, *127*, 3928–3934.
- (9) Gao, J.; Liang, G.; Zhang, B.; Kuang, Y.; Zhang, X.; Xu, B. FePt@CoS₂ Yolk-Shell Nanocrystals as a Potent Agent to Kill HeLa Cells. *J. Am. Chem. Soc.* **2007**, *129*, 1428–1433.
- (10) Lee, N.; Cho, H. R.; Oh, M. H.; Lee, S. H.; Kim, K.; Kim, B. H.; Shin, K.; Ahn, T.-Y.; Choi, J. W.; Kim, Y.-W.; Choi, S. H.; Hyeon, T. Multifunctional Fe₃O₄/TaO_x Core/Shell Nanoparticles for Simultaneous Magnetic Resonance Imaging and X-ray Computed Tomography. *J. Am. Chem. Soc.* **2012**, *134*, 10309–10312.
- (11) Verdaguier-Casadevall, A.; Deiana, D.; Karamad, M.; Siahrostami, S.; Malacrida, P.; Hansen, Th. W.; Rossmeisl, J.; Chorkendorff, I.; Stephens, I. E. L. Trends in Electrochemical Synthesis of H₂O₂: Enhancing Activity and Selectivity by Electrocatalytic Site Engineering. *Nano Lett.* **2014**, *14*, 1603–1608.
- (12) Zeng, H.; Li, J.; Wang, Z. L.; Liu, J. P.; Sun, S. Bimagnetic Core/Shell FePt/Fe₃O₄ Nanoparticles. *Nano Lett.* **2004**, *4*, 187–190.
- (13) Baumbach, G. T.; Tixier, S.; Pietsch, U.; Holy, V. Grazing Incident Diffraction from Multilayers. *Phys. Rev. B: Condens. Matter Mater. Phys.* **1995**, *51*, 16848–16859.
- (14) Renaud, G.; Lazzari, R.; Leroy, F. Probing Surface and Interface Morphology with Grazing Incidence Small Angle X-Ray Scattering. *Surf. Sci. Rep.* **2009**, *64*, 255–380.
- (15) Browning, N. D.; Pennycook, S. J. Direct Experimental Determination of the Atomic-Structure at Internal Interfaces. *J. Phys. D: Appl. Phys.* **1996**, *29*, 1779–1798.
- (16) Lamberti, C. The Use of Synchrotron Radiation Techniques in the Characterization of Strained Semiconductor Heterostructures and Thin Films. *Surf. Sci. Rep.* **2004**, *53*, 1–197.
- (17) Daweritz, L.; Ploog, K. Contribution of Reflection High-Energy Electron Diffraction to Nanometre Tailoring of Surfaces and Interfaces by Molecular Beam Epitaxy. *Semicond. Sci. Technol.* **1994**, *9*, 123–136.
- (18) Petkov, V. Nanostructure by High-Energy XRD. *Mater. Today* **2008**, *11*, 28–38.
- (19) Bell, A. T. The Impact of Nanoscience on Heterogeneous Catalysis. *Science* **2003**, *299*, 1688–1691.
- (20) Sato, K. Magnetic Nanoparticles: When Atoms Move Around. *Nat. Mater.* **2009**, *8*, 924–925.
- (21) Alivisatos, A. P. Perspective on the Physical Chemistry of Semiconductor Crystals. *J. Phys. Chem.* **1996**, *100*, 13226–13239.
- (22) Ozbay, E. Plasmonics: Merging Photonics and Electronics at Nanoscale Dimensions. *Science* **2006**, *311*, 189–193.
- (23) LaVan, D. A.; McGuire, T.; Langer, R. Small-Scale Systems for in Vivo Drug Delivery. *Nat. Biotechnol.* **2003**, *21*, 1184–1191.
- (24) Chen, C.-Y.; Lai, W.-H.; Yan, W.-M.; Chen, C.-C.; Hsu, S.-W. Effects of Nitrogen and Carbon Monoxide Concentrations on Performance of Proton Exchange Membrane Fuel Cells with Pt-Ru Anodic Catalyst. *J. Power Sources* **2013**, *243*, 138–146.
- (25) Alayoglu, S.; Zavalij, P.; Eichhorn, B.; Wang, Q.; Frenkel, A. I.; Chupas, P. Structural and Architectural Evaluation of Bimetallic Nanoparticles: A Case Study of Pt-Ru Core-Shell and Alloy Nanoparticles. *ACS Nano* **2009**, *3*, 3127–3137.
- (26) Hsieh, Y.-C.; Zhang, Y.; Su, D.; Volkov, V.; Si, R.; Wu, L.; Zhu, Y.; An, W.; Liu, P.; He, P.; Ye, S.; Adzic, R. R.; Wang, J. X. Ordered Bilayer Ruthenium-Platinum Core-Shell Nanoparticles as Carbon Monoxide-Tolerant Fuel Cell Catalyst. *Nat. Commun.* **2013**, *4*, 2446.
- (27) Rabis, A.; Rodriguez, P.; Schmidt, T. J. Electrocatalysis for Polymer Electrolyte Fuel Cells: Recent Achievements and Future Challenges. *ACS Catal.* **2012**, *2*, 864–890.
- (28) Wiltshire, R. J.K.; King, C. R.; Rose, A.; Wells, P. P.; Davies, H.; Hogarth, M. P.; Thompsett, D.; Theobald, B.; Mosselmann, F. W.; Roberts, M.; Russell, A. E. Effects of Composition on Structure and Activity of PtRu/C Catalysts. *Phys. Chem. Chem. Phys.* **2009**, *11*, 2305–2313.
- (29) Chen, T.-Y.; Lin, T.-L.; Luo, T.-J. M.; Choi, Y.; Lee, J.-F. Effects of Pt Shell Thickness on the Atomic Structure of Ru-Pt Core-Shell

Nanoparticles for Methanol Electrooxidation Applications. *ChemPhysChem* **2010**, *11*, 2383–2392.

(30) Watanabe, M.; Motoo, S. Electrocatalysis by Ad-Atoms: Part III. Enhancement of the Oxidation of Carbon Monoxide on Platinum by Ruthenium Ad-Atoms. *J. Electroanal. Chem. Interfacial Electrochem.* **1975**, *60*, 275–283.

(31) Gasteiger, H. A.; Markovic, N.; Ross, P. N.; Cairns, E. J. CO Electrooxidation on Well-Characterized Pt-Ru Alloys. *J. Phys. Chem.* **1994**, *98*, 617–625.

(32) Fuoss, P. H.; Eisenberger, P.; Warburton, W. K.; Bienenstock, A. Application of Differential Anomalous X-Ray Scattering to Structural Studies of Amorphous Materials. *Phys. Rev. Lett.* **1981**, *46*, 1537–1540.

(33) Waseda, Y. in *Novel Applications of Anomalous (Resonance) X-Ray Scattering for Characterization of Disordered Materials*; Springer: Berlin, 1984.

(34) Frenkel, A. Solving the 3D Structure of Metal Nanoparticles. *Zeitschrift für Kristallographie* **2007**, *222*, 605–611.

(35) Klug, P. K.; Alexander, L. E. *X-Ray Diffraction Procedures: For Polycrystalline and Amorphous Materials*, 2nd ed.; Wiley-Interscience: New York, 1974.

(36) Petkov, V.; Shastri, S.; Shan, S.; Joseph, P.; Luo, J.; Zhong, C.-J.; Nakamura, T.; Herbani, Y.; Sato, S. Resolving Atomic Ordering Differences in Group 11 Nanosized Metals and Binary Alloy Catalysts by Resonant High-Energy X-ray Diffraction and Computer Simulations. *J. Phys. Chem. C* **2013**, *117*, 22131–22141.

(37) Petkov, V.; Wanjala, B. N.; Loukrakpam, R.; Luo, J.; Yang, L.; Zhong, C.-J.; Shastri, S. Pt-Au Alloying at the Nanoscale. *Nano Lett.* **2012**, *12*, 4289–4299.

(38) Bedford, N.; Viau, G.; Chupas, P.; Petkov, V.; Dablenmont, C. 3D structure of Nanosize Catalysts by High-Energy X-ray Diffraction and Reverse Monte Carlo Simulations: Study of Ru. *J. Phys. Chem. C* **2007**, *111*, 18214–18219.

(39) Pearson, W. B. *The Crystal Chemistry and Physics of Metals and Alloys*; Wiley-Interscience: New York, 1972.

(40) Petkov, V.; Shan, S.; Chupas, P.; Yin, J.; Yang, L.; Luo, J.; Zhong, C. J. Noble-Transition Metal Nanoparticle Breathing in a Reactive Gas Atmosphere. *Nanoscale* **2013**, *5*, 7379–7387.

(41) Farrow, L.; Juhas, P.; Liu, J.; Bryndin, D.; Bozin, E.; Bloch, J.; Proffen, T.; Billinge, S. PDFfit2 and PDFgui: Computer Programs for Studying Nanostructure in Crystals. *J. Phys.: Condens. Matter* **2007**, *219*, 335219.

(42) Note: The contribution of Pt–Pt atomic pair correlations to the experimental Pt-differential PDFs shown in Figure 3a is somewhat larger than that of Pt–Ru ones since Pt atoms scatter X-rays stronger than Ru ones.

(43) Pt-differential PDFs for Pt₃₁Ru₆₉ and Pt₇₅Ru₂₅ alloy NPs decay gradually with interatomic distances but at different rates since the relative concentration of Pt species in the respective NPs is different.

(44) Note: The different phase state (partially segregated vs single phase) of Pt₃₁Ru₆₉ and Pt₇₅Ru₂₅ alloy NPs may not come as a big surprise. That is because when alloyed in bulk, fcc Pt and hcp Ru do not form a continuous solid solution even when annealed at temperature above 1000 oC [e.g., see Hutchinson, J. M. Platinum-Ruthenium Binary Alloy Phase Diagram. *Platinum Met. Rev.* **1972**, *16*, 88–90]. In particular, bulk Pt–Ru alloys containing less than 50 at % of Ru tend to crystallize in an fcc-type structure. On the other hand, bulk Pt–Ru alloys containing more than 80 at % of Ru tend to crystallize in a hcp-type structure. Bulk Pt–Ru alloys containing 50–80 at % Ru tend to segregate into coexisting Ru-rich and Pt-rich phases of a hcp- and fcc-type structure, respectively. Evidently, Pt₃₁Ru₆₉ and Pt₇₅Ru₂₅ alloy NPs studied here reproduce the phase state of their bulk counterparts.

(45) Note: Other studies [e.g., Ruban, A.V.; Skriver, H.L.; Norskov, J.K. Surface segregation energies in transition-metal alloys. *Phys. Rev. B* **1999**, *59*, 15990–16000; Hill, Ch. W.; Nasher, M.S.; Frenkel, A. I.; Shapley, J. R.; and Nuzzo, R. G. Carbon support effect on bimetallic Pt–Ru Nanoparticles Formed from molecular precursors. *Langmuir* **1999**, *15*, 690–700] on Pt–Ru alloy NPs of low Pt content have also found a tendency of Pt species to segregate at the NP surface and

explained it with the fact that the surface energy of Pt (2.7 J/m²) is lower than that of Ru (3.4 J/m²).

(46) Bochicchio, D.; Ferrando, R. Morphological Instability of Core-Shell Metallic Nanoparticles. *Phys. Rev. B: Condens. Matter Mater. Phys.* **2013**, *87*, 165435.

(47) Wales, D. J.; Doye, J. P. K. Global Optimization by Basin-Hopping and the Lowest Energy Structures of Lennard-Jones Clusters Containing up to 110 Atoms. *J. Phys. Chem. A* **1997**, *101*, 5111–5116.

(48) Petkov, V.; Prasai, B.; Ren, Y.; Shan, S.; Luo, J.; Joseph, P.; Zhong, C.-J. Solving the Nanostructure Problem: Exemplified on Metallic Alloy Nanoparticles. *Nanoscale* **2014**, *6*, 10048–10061.

(49) Norskov, J. K.; Bligaard, T.; Rossmeisl, J.; Christensen, C. H. Towards the Computational Design of Solid Catalysts. *Nat. Chem.* **2009**, *1*, 37–46.

(50) Schlapka, A.; Lischka, M.; Gros, A.; Kasberger, U.; Jacob, P. Surface Strain versus Substrate Interaction in Heteroepitaxial Metal Layers: Pt on Ru (0001). *Phys. Rev. Lett.* **2003**, *91*, 016101.

(51) Nilekar, A. U.; Alayoglu, S.; Eichhorn, B.; Mavrikakis, M. Preferential CO oxidation in Hydrogen: Reactivity of Core-Shell Nanoparticles. *J. Am. Chem. Soc.* **2010**, *132*, 7418–7428.

(52) Alayoglu, S.; Nilekar, A. U.; Mavrikakis, M.; Eichhorn, B. Ru-Pt Core-Shell Nanoparticles for Preferential Oxidation of Carbon Monoxide in Hydrogen. *Nat. Mater.* **2008**, *7*, 333–338.

(53) Hammer, B.; Norskov, J. K. Theoretical Surface Science and Catalysis – Calculations and Concepts. *Adv. Catal.* **2007**, *45*, 71–129.

(54) Kitchin, J. R.; Norskov, J. K.; Barteau, M. A.; Chen, J. G. Role of Strain and Ligand Effects in the Modification of the Electronic Structure and Chemical Properties of Bimetallic Substrates. *Phys. Rev. Lett.* **2004**, *93*, 156801.

(55) Pauling, L. *The Nature of the Chemical Bond*. Cornell University Press: Ithaca, NY, 1975.

(56) Pauling, L. Factors Determining the Average Atomic Volumes in Intermetallic Compounds. *Proc. Natl. Acad. Sci. U. S. A.* **1987**, *84*, 4754–4756.

(57) Rajasekharan, T.; Seshubai, V. Charge Transfer on the Metallic Atom-Pair Bond, and the Crystal Structures Adopted by Intermetallic Compounds. *Acta Crystallogr., Sect. A: Found. Crystallogr.* **2012**, *68*, 156–165.

(58) Mavrikakis, M.; Hammer, B.; Norskov, J. K. Effect of Strain on the Reactivity of Metal Surfaces. *Phys. Rev. Lett.* **1998**, *13*, 2819.

(59) Gasteiger, H. A.; Kocha, S. S.; Sompalli, B.; Wagner, F. T. Activity Benchmarks and Requirements for Pt, Pt-alloys, and non-Platinum ORR Catalysts for PEMFCs. *Appl. Catal., B* **2005**, *56*, 9–35.

(60) Calderon, J. C.; Garcia, G.; Rodriguez, J. L.; Lazaro, M. J.; Pastor, E.; Calvillo, L. Electrochemical Oxidation of CO and Methanol on Pt–Ru Catalysts Supported on Carbon Fibers: the Influence of Synthesis Method. *Appl. Catal., B* **2015**, *165*, 676–686.

(61) Huang, S.-Y.; Chang, S.-M.; Lin, C.-L.; Chen, C.-H.; Yeh, C.-T. Promotion of the Electrochemical Activity of Bimetallic Pt–Ru Catalysts by Oxidation-induced Segregation. *J. Phys. Chem. B* **2006**, *110*, 23300–23305.

(62) Scott, F. J.; Mukerjee, S.; Ramaker, D. E. CO Coverage/Oxidation with PtRu Electrocatalyst Particle Morphology in 0.3M Methanol by in situ XAS. *J. Electrochem. Soc.* **2007**, *154*, A396–A406.

(63) Tripkovic, A. V.; Popovic, K. D.; Grgur, B. N.; Bliznac, B.; Ross, P. N.; Marcovic, N. M. Methanol Electrooxidation on Supported Pt and PtRu Catalysts in Acid and Alkaline Solutions. *Electrochim. Acta* **2002**, *47*, 3707–3714.

(64) Chen, D.; Li, Y.; Liao, Sh, Su D.; Song, H.; Li, Y.; Yang, L.; S, D.; Li, C. Ultra-high-performance core-shell Ru@Pt/C Catalysts Prepared by a Facile Pulse Electrochemical Deposition Method. *Sci. Rep.* **2015**, *5*, 11604.

(65) Hoster, H. E.; Alves, O. B.; Koper, M. T. M. Tuning Absorption via Stress and Vertical Ligand Effect. *ChemPhysChem* **2010**, *11*, 1518–1524.

(66) Carter, E. A. Challenges in Modeling Materials Properties without Experimental Input. *Science* **2008**, *321*, 800–803.

(67) Quek, X.-Y.; Pilot, I. A.; Pestman, R.; van Santen, R. A.; Petkov, V.; Hensen, E. J. Correlating Fischer–Tropsch Activity to Ru

Nanoparticle Surface Structure as Probed by High-Energy XRD. *Chem. Commun.* **2014**, *50*, 6005–6008.

(68) Note: In general, XRD is bulk sensitive technique. Therefore, high-energy XRD patterns and respective experimental atomic PDFs are sensitive to the atomic arrangement of surface atoms in 5–7 nm size particles, including atomic pair distances and coordination numbers, because surface atoms in such NPs constitute up to about 30% of particle's volume.

(69) Jackson, A.; Viswanathan, V.; Forman, A. J.; Larsen, A. H.; Norskov, J. K.; Jaramillo, T. F. Climbing the Activity Volcano: Core-Shell Ru@Pt Electrocatalysts for Oxygen Reduction. *ChemElectroChem* **2014**, *1*, 67–71.

(70) Morozan, A.; Jusselme, B.; Palacin, S. Low-Platinum and Platinum-Free Catalysts for the Oxygen Reduction Reaction at Fuel Cell Cathodes. *Energy Environ. Sci.* **2011**, *4*, 1238–1254.

(71) Peng, Z.; Freunberger, S. A.; Chen, Y.; Bruce, P. G. A Reversible and Higher-Rate Li-O₂ Battery. *Science* **2012**, *337*, 563–566.

(72) Chen, T.-Y.; Chen, I.-L.; Liu, Y.-T.; Lin, T.-L.; Yang, P.-W.; Wu, C.-Y.; Hu, C.-C.; Luo, T.-J. M.; Lee, C.-H. Core-Dependent Growth of Pt Shell Nanocrystals and their Electrochemical Characteristics for Fuel Cells. *CrystEngComm* **2013**, *15*, 982–994.